The effects of gradient index, aspect ratio, porosity, and boundary conditions on the buckling behavior of functionally graded porous beams: A *k-out-of-n* system reliability analysis

Ravikiran Chintalapudi [a], Geetha Narayanan Kannaiyan [b], Bridjesh Pappula [c], Seshibe Makgato [c,*]

[a] *Department of Mechanical Engineering, MLR Institute of Technology, Hyderabad 500043, India*
[b] *Department of Mathematics, Dayananda Sagar College of Engineering, Bengaluru 560078, India*
[c] *Department of Chemical Engineering, College of Science, Engineering and Technology, University of South Africa (UNISA), C/o Christiaan de Wet & Pioneer Avenue, Florida Campus, 1710 Johannesburg, South Africa*

ARTICLE INFO

ABSTRACT

Functionally graded materials are a class of multifunctional materials that exhibit spatial variation in composition and microstructure. This deliberate variation is designed to effectively manage and manipulate changes in thermal, structural, or functional qualities within the material. The current study explores the system reliability of functionally graded porous beams (FGPB) subjected to buckling, focusing on the interplay of gradient index (0, 0.5, 1, 2, 3, 4, 5, 6, 7, 8, 9 and 10), aspect ratio (5, 10, 15, 20, 25, 30 and 35), porosity index (0, 0.1 and 0.2) and boundary conditions (simply supported, clamped–clamped and clamped-free), with a particular emphasis on the *k-out-of-n* system reliability assessment, employing three distinct methods such as Evolutionary, GRG Non-linear, and Lagrangian. The results show the system's sensitivity to changes in distribution parameters, with the Lagrangian method being the most robust and stable. The *10-out-of-12* system reliability analysis demonstrates that aspect ratio and even porosity distribution are reliable, while uneven porosity is not. This study enhances structural reliability analysis in FGPBs, enhancing system reliability considerations and paving the way for further advancements in structural reliability analysis.

Introduction

In engineering applications, composite materials must be created by combining materials in either solid or molten states, within the constraints of thermodynamic equilibrium limits. Functional gradients are composite materials designed to tackle issues in laminates, especially at interfaces were stress changes abruptly, causing failure. These materials, known as functionally graded materials (FGM), blend different materials in varying proportions along one or more spatial coordinates, resulting in unique properties [1]. Functionally graded porous material (FGPM) is characterized by its numerous interior pores, which can occur either during the sintering process or can be intentionally introduced in specific distribution patterns. The distribution of these pores within the structure can take various forms, such as uniform, non-uniform, trigonometric, and exponential distributions [2]. The salient characteristics of porous composites are their notable and varied geometries, namely

the distributions of material, which provide distinct opportunities for the design and enhancement of densities. The unique characteristics of this FGPM are directly associated with the shape of its interior pores, resulting in exceptional mechanical, thermal, chemical, biological and electrical properties, hence enhancing its attractiveness [3–5]. The use of graded material compositions and the manipulation of porosity distributions result in the emergence of innovative multifunctional advantages. The majority of porous composites used for load-bearing applications are typically analysed with the assumption that the void spaces contain only dry air. In contrast to the comparatively intricate and expensive process of integrating two distinct materials, it is simpler and more feasible to fabricate modifications in cellular morphologies. Furthermore, these modifications exhibit exceptionally appealing properties. Numerous investigations have incorporated uniform and non-uniform internal pores into metal-ceramic composites, in which the structural thickness is traversed by functionally graded porosities and metals and ceramics are abundant on opposing surfaces. Karami et al.

Nomenclature

ANN	Artificial neural network
CC	Clamped-clamped
CF	Clamped-free
CNTRC	Carbon nanotube-reinforced composite
EBT	Euler-Bernoulli beam theory
FEM	Finite element method
FGB	Functionally graded beam
FGM	Functionally graded material
FGP	Functionally graded plate
FGPB	Functionally graded porous beam
FGPM	Functionally graded porous material
FGPTB	Functionally graded porous Timoshenko beam
FSDT	First order shear deformation theory
GDQM	Generalized differential quadrature method
GRG	Grey relational grade
HSDT	Higher order shear deformation theory
KT	Kuhn-Tucker
MTTF	Mean time to failure
RR	The reliability range
S-FGM	Sigmoid functionally graded material
SS	Simply supported
TBT	Timoshenko beam theory
b	The width of the beam
c	The presence of ceramic.
h	The thickness of the beam
L	The length of the beam
m	The presence of metal
α	The porosity coefficient ($0 \leq \alpha \leq 0.4$)
$O(x,y,z)$	Origin in the Co-ordinate system
V_f	Volume fraction of a constituent
P_x	The gradient index in the direction of the beam's length.
P_z	The gradient index in the direction of the beam's thickness.
P_c	The material properties of ceramic
P_m	The material properties of metal
$P_{x,z}$	Effective material properties on the beam
$U(x,z)$	Axial displacements
$W(x,z)$	Transverse displacement
u_0	Axial displacement at the given point
w_0	Transverse displacement at the given point
$\frac{\partial w_0}{\partial x}$	Bending slope
$\varnothing$	The shear slope
$f(z)$	The shear shape function
ε_x	Non- zero axial strain
γ_{xz}	Non- zero shear strain
σ_x	Unilateral stress
τ_{xz}	Shear stress
δU	The potential energy of the strain
δK	The kinetic energy of the strain
M_x	The bending moment
N_x	The total axial force
P_x, Q_x, R_x	The higher order stress resultants
$q(x)$	The transverse load
∂V	The potential work
π	The total potential energy
U^0	Lagrange multiplier
$\theta_i, \varphi_i, \psi_i$	The boundary conditions
λ	The scalar
$\overline{N}_{cr}$	The non-dimensional critical buckling
N_{cr}	The critical buckling
L/h	The aspect ratio
$R(t)$	The system reliability
$N_s(t)$	The number of components that are operating at time t
$N_f(t)$	The number of components that have failed at time t
$\lambda(t)$	The failure rate

[6] studied wave propagation on porous nanoplates using FSDT and nonlocal elasticity theories, considering factors such as material gradation and wave number. Ebrahimi et al. [7] developed a framework for thermo-mechanical dynamic properties of smart shear-deformable piezoelectric nanobeams made of porous electro-elastic FGMs, analysing electro-elastic characteristics and influencing parameters.

Fiber-reinforced laminated composites are increasingly used in engineering due to advancements in production technology. However, porosities can occur during production, causing significant changes in composite properties. Yüksel and Akbaş [8] conducted a buckling study on a laminated composite plate reinforced with fibers, analysing the effects of porosity using the FSDT on plates. They used three distinct porosity models and the Navier approach to solve the problem. Berghouti et al. [9] explored the dynamic behaviour of functionally graded porous nano-beams using a nonlocal nth-order shear deformation theory. Kiarasi et al. [10] analysed the natural frequency of a porous nanocomposite shell reinforced with graphene platelets. Akbas et al. [11] studied the dynamic responses of a composite thick beam with three porous layers under a dynamic sine pulse load, considering material gradation and porosity distributions. Alnujaie et al. [12] studied the forced dynamic response of a thick FGB supported by a viscoelastic foundation, demonstrating high efficiency in applications using porous fiber-reinforced materials. Akbas [13] studied shifting load in FGBs using Lagrange and Ritz techniques, while Alimoradzadeh and Akbas [14] analysed nonlinear vibration in a composite beam with carbon nanotubes and a viscoelastic foundation. Bensaid and Saimi [15] used the GDQM to analyse a viscoelastic beam made of porous FGM, evaluating material characteristics and examining factors such as porosity

distribution, foundation type and structural damping coefficient. Bentrar et al. [16] conducted a free vibration analysis on FGM sandwich plates with porosity using FEM and FSDT. Bourada et al. [17] used a unique four-variable integral quasi-3D HSDT to analyse wave propagation in imperfect functionally graded sandwich plates. Addou et al. [18] studied the bending behaviour of a porous FGM plate using a unique higher quasi-3D hyperbolic shear deformation theory. Alsubaie et al. [19] studied the vibration response of a CNTRC beam using simplified HSDT and found that porosity significantly influences beam vibrational properties. Khorasani et al. [20] studied the vibrational characteristics of FGPTBs and found enhanced rigidity.

Mechanical models have been used to study the operational characteristics of porous structures, such as functionally graded porous beams (FGPBs). These models have been developed using various techniques, such as finite element modelling (FEM) [21], artificial neural network (ANN) techniques [36] and polynomial series functions [37]. The impact of porosity distribution patterns on FGPB characteristics has also been explored. Factors such as side-to-thickness ratio, aspect ratio, material index, loading type, porosity and foam shapes have also been found to influence critical buckling behavior. Mesbah et al. [21] studied FGPB behaviour under vibration and buckling scenarios using FEM. They also explored the impact of porosity distribution patterns on FGPB characteristics. Kativar et al. [22] developed a porosity model for a bi-directional plate with geometric imperfections and porosities. Cuong-Le et al. [23] investigated the linear and nonlinear solutions of a S-FGM nanoplate with porous effects, examining two distinct patterns of porosity distribution. Xia et al. [24] studied free vibration in porous shell panels reinforced with graphene platelets, revealing that

nanofiller weight significantly affects shell dynamic response. Belabed et al. [25] developed a beam finite element model for porous structures, while Chitour et al. [26] studied the impact of porosity on sandwich plate stability under mechanical loading conditions. Chen et al. [27] conducted a study using finite element homogenization and structural evaluations to study the buckling and vibration characteristics of laminated FGP made of closed-cell foams. They predicted the foam Young's modulus using representative volume elements and validated the results. The presence of graded porosities was found to increase beam stiffness and the critical buckling load, suggesting they are associated with closed-cell aluminium foams. In recent years, both analytical [28,29] and numerical [30,31] analyses of the mechanical properties of FG porous composite structures have become more popular. This is because the described FGP can be used on a wider range of structural forms. The functionally graded beam [32], plate [33], tube [34], arch [35] and shell are representative instances that exhibit diverse porosity distributions along the direction of thickness. These variations give rise to graded material properties and, as a result, contribute to the overall improvement in performance. Turan et al. [36] developed an analytical solution using first-order shear deformation theory to analyse free vibration and buckling behaviour of FGPBs under different boundary conditions [37]. Derikvand et al. [38] investigated the buckling properties of a sandwich beam with a porous ceramic core, finding that the critical buckling stress of a three-layer beam surpasses other configurations. Wang et al. [39] examined the bending and buckling properties of nanobeams, focusing on porosity distribution.

Mechanical models have been used to study the operational characteristics of porous structures. Turan et al. [36] developed an analytical solution using first-order shear deformation theory to analyse free vibration and buckling behaviour of FGPBs under different boundary conditions [38]. Derikvand et al. [37] investigated the buckling properties of a sandwich beam with a porous ceramic core, finding that the critical buckling stress of a three-layer beam surpasses other configurations. Wang et al. [39] examined the bending and buckling properties of nanobeams, focusing on porosity distribution. The structural integrity of complex materials like FGBs depends on reliability assessment. As Truong et al. [40] and Nguyen-Xuan et al. [41] have shown, probabilistic methods have advanced dependability analysis. Wang et al. [42] have developed a machine learning-assisted method for structural analysis of functionally graded structures under static loads. They incorporated uncertain system factors like material qualities, dimensions, applied loads, and FGM degree. The 3D finite element technique and the extended support vector regression strategy describe the link between structural behaviours and uncertain system inputs. Lieu et al. [43] developed a reliability-based design optimization technique for multidirectional functionally graded plates. They created two distinct non-uniform rational B-spline surfaces using a refinement procedure that reduced design variables and computing costs while accurately reproducing the plate's mechanical properties. FGPBs are used in various engineering fields, including aerospace [44], automotive [45], biomedical [46] and civil engineering [47]. For example, in aerospace, lightweight, structurally robust components are needed for wing spars. A bi-directional functionally graded porous beam is designed to optimize mechanical properties, enhancing stiffness, strength and toughness while minimizing weight.

Despite significant progress in understanding and highlighting the achievements linked to studies on FGMs and FGPMs, several remaining gaps require further research. While previous studies have investigated these components individually, comprehensive investigations that integrate all of them into a framework for reliability analysis are not present. To the best of the authors knowledge, integrating multiple variables into a unified analysis provides a more holistic understanding of the structural response. In addition, there isn't much research on how to use a k-out-of-n system reliability analysis to test the structural dependability of FGPBs in different situations. This would allow the analysis to go further and figure out the likelihood of failure and the most important factors that affect reliability. The study aims to investigate the impact of aspect ratio on structural dependability in FGPBs. It establishes a model using HSDT to integrate the properties of alumina and aluminum and solves governing equations for different boundary conditions to determine non-dimensional critical buckling loads. The study also assesses the system reliability of the beams using Evolutionary, GRG Non-linear, and Lagrangian approaches, as well as applying a *k-out-of-n* system reliability analysis.

Methodology

Model of a FGPB

FGPB, represented in Fig. 1, is a slender structural component capable of bending and shearing. The beam is postulated to exhibit linearity and straightness along its entire length, incorporating minor deformations and linearized equations. The influence of warping effects resulting from cross-sectional twisting is neglected, and it is assumed that cross-sections that were initially plane maintain their planeness even after undergoing deformation. FGPB with length *L*, width *b*, and thickness *h* is considered, and the origin 'O' is chosen with the coordinate system O(*x,y,z*). The top side of the beam is composed of ceramic (c) while metal (m) is at the bottom.

Material properties

Power law distribution is applied to estimate the volume fraction of each constituent and can be expressed as in Eqs. (1a) and (1b).

$$V_{f1}(x,z) = \left(\frac{z}{h} + \frac{1}{2}\right)^{P_z}\left(\frac{x}{L} + \frac{1}{2}\right)^{P_x} \tag{1a}$$

$$V_{f1}(x,z) + V_{f2}(x,z) = 1 \tag{1b}$$

where P_x, and P_z are gradient indices, and the length of the varies as $0 \leq x \leq 1$ and the thickness varies as $0 \leq z \leq$ h. The effective material properties of evenly and unevenly distributed FGPB can be estimated using Eqs. (2a) and (2b), respectively.

$$P_{x,z} = (P_c - P_m)\left(\frac{z}{h} + \frac{1}{2}\right)^{P_z}\left(\frac{x}{L} + \frac{1}{2}\right)^{P_x} + P_m - \frac{\alpha}{2}(P_c + P_m) \tag{2a}$$

$$P_{x,z} = (P_c - P_m)\left(\frac{z}{h} + \frac{1}{2}\right)^{P_z}\left(\frac{x}{L} + \frac{1}{2}\right)^{P_x} + P_m - \frac{\alpha}{2}(P_c + P_m)\left(1 - \frac{2|z|}{h}\right) \tag{2b}$$

where α denotes the porosity coefficient, $0 \leq \alpha \leq 0.4$.

Aluminum and alumina have numerous applications in structural analysis, and so they are used as structural materials in the present study. Aluminum and alumina are utilized in aerospace engineering, where lightweight and durable components are critical, to evaluate the structural integrity of aircraft components such as fuselages and wings. In a similar manner, beams play a critical role in the fabrication of bridges and structures within the fields of civil engineering and architecture. These materials are frequently employed by mechanical engineers in apparatus and systems, with their strength being guaranteed through the application of beam theory to enhance design. Aluminum alloys also benefit the automotive industry through the reduction of component weight and the enhancement of fuel economy. Due to its exceptional resistance to corrosion, aluminum is an essential material in maritime engineering for vessels and ships. In conjunction with beam theory, aluminum and alumina enable the evaluation and enhancement of structural performance in a vast array of industries and applications. The properties of aluminum and alumina are presented in Table 1.
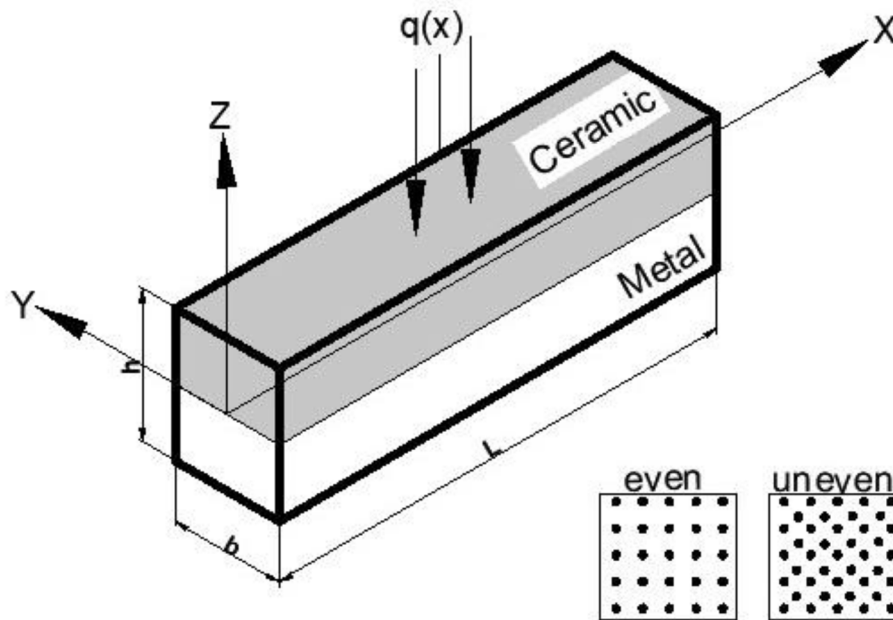
Fig. 1. FGPB, with even and uneven porosity.

Table 1
Properties of constituent material- aluminum and alumina [48].

Constituent	Young's modulus (GPa)	Poisson's ratio
Aluminum	70	0.3
Alumina	380	0.3

Displacement field and equilibrium equation

The displacement field equations elucidate the manner in which locations inside the FGPB undergo deformation when subjected to external loads or boundary conditions. These findings offer information on how displacements are distributed throughout the length, radial and transverse directions of the beam. They take into account changes in material qualities and geometrical parameters across the beam's cross-section. The displacement field that fulfils the beam's postulates is determined by the constitutive equations, denoted as Eqs. (3a), (3b) [49].

$$U(x,z) = u_0(x) + z\varnothing(x) - f(z)\left(\varnothing(x) + \frac{\partial w_0}{\partial x}(x)\right) \tag{3a}$$

$$W(x,z) = w_0(x) \tag{3b}$$

where axial as well as transverse displacements are represented by U and W respectively, at any point (x,z). At any given position along the neutral axis, u_0 and w_0 represent the axial as well as transverse displacements, respectively. The bending slope is denoted by $\frac{\partial w_0}{\partial x}$, and $\varnothing$ the shear slope.

HSDTs use shear shape functions to better predict thin-walled objects' mechanical responses. These shape functions improve analytical predictions by adding transverse shear deformation and properly characterizing shear stresses throughout thickness. This allows for more precise and reliable structural behavior predictions in various engineering applications. In the present study, the shear shape function f(z) used is shown in Eq. (4) [50].

$$f(z) = \frac{4z}{h} - \frac{16z^3}{3h^3} \tag{4}$$

$f(z)$ describes the variation of the radial displacement with respect to the distance from the neutral axis of the FGPB. $\frac{4z}{h}$ represents the linear variation of the radial displacement with respect to the distance from the neutral axis. As z increases, the radial displacement increases linearly, with the rate of increase determined by the ratio, $\frac{z}{h}$. $-\frac{16z^3}{3h^3}$ represents a cubic variation of the radial displacement with respect to the distance from the neutral axis, which introduces nonlinearity in the displacement profile and a bending effect in the deformation of the beam. As z increases, the magnitude of the cubic term also increases, leading to a more pronounced curvature in the radial displacement profile. The deformation behavior is more precisely represented by this shear shape function, which incorporates both linear as well as nonlinear components with the application of boundary conditions. Non-zero strain terms denote the tangible deformations encountered by the material when subjected to a load. These deformations encompass alterations in length, shape, and distortion caused by shear forces. By differentiating Eqs. (3a), (3b) and (4), the non-zero axial and shear strains are derived and presented in Eqs. (5a) and (5b).

$$\varepsilon_x = \frac{\partial U}{\partial x} = \frac{\partial u_0}{\partial x} + z\frac{\partial \varnothing}{\partial x} - f(z)\left(\frac{\partial \varnothing}{\partial x} + \frac{\partial^2 w_0}{\partial x^2}\right) \tag{5a}$$

$$\gamma_{xz} = (1 - f')(\varnothing + \frac{\partial w_0}{\partial x}) \tag{5b}$$

The linear correlation between strain and stress in an elastic material is characterized by Hooke's Law. For a uniaxial stress (σ_x) along the x-direction and a shear stress (τ_{xz}), Hooke's law can be applied to establish the relation between (σ_x) and (τ_{xz}) as presented in Eqs. (6a) and (6b).

$$\sigma_x = E(x)\varepsilon_x \tag{6a}$$

$$\tau_{xz} = \frac{E(x)}{2(1+\mu)}\gamma_{xz} \tag{6b}$$

The strain energy in a FGPB is derived by integrating the strain energy density (∂U) over the volume of the beam using Eq. (7).

$$\partial U = \int_0^L \int_A \left(\sigma_x \varepsilon_x + \tau_{xz} \gamma_{xz} \right) dz dx \qquad (7)$$

by substituting Eqs. (5a), (5b), (6a), and (6b) in Eq. (7), the resulting strain energy can be expressed as,

$$\partial U = \int_0^L \int_A \left\{ \sigma_x \left[\frac{du_o}{dx} + z\frac{d\varnothing}{dx} - f(z)\left(\frac{d\varnothing}{dx} + \frac{\partial^2 w_0}{\partial x^2} \right) \right] + \sigma_{xz} \left[\left(1 - \frac{4}{h} + \frac{16z^2}{h^3} \right) \left(\varnothing + \frac{\partial w_0}{\partial x} \right) \right] \right\} dA dx \qquad (8)$$

when N_x is the total axial force acting on the cross-section of the beam, M_x is the total bending moment about the neutral axis of the beam, P_x, Q_x and R_x are higher-order stress resultants to capture the additional effects beyond the conventional axial force and bending moment. These variables are of utmost importance in the examination and development of beams, as they offer valuable understanding regarding the dispersion of internal forces as well as stresses that govern the beam's characteristics and reaction to external loads.

$$N_x = \int_A \sigma_x dA$$

$$M_x = \int_A z\sigma_x dA$$

$$P_x = \int_A z^3 \sigma_x dA$$

$$R_x = \int_A z^2 \sigma_{xz} dA$$

$$Q_x = \int_A \sigma_{xz} dA$$

The potential work for the transverse load applied, $q(x)$ acting on the FGPB, resulting in a displacement w_0 at each point along the length of the beam, is expressed in Eq. (9). The negative symbol signifies that this work is being performed against the exerted force. In the principle of virtual work, this is used to determine the displacements and deformations in structural analysis by considering the equilibrium of virtual displacements.

$$\partial V = -\int_0^L q(x) w_0 dx \qquad (9)$$

Applying the principle of virtual displacement and adapting the principle of minimum potential energy, the total potential energy (π) captures the balance between the internal strain energy stored within the structure and the external work done by the applied loads and is estimated as given in Eq. (10). By utilizing this principle, it becomes possible to assess the equilibrium state of the structure through an analysis of potential energy fluctuations related to virtual displacements. It is possible to ascertain the equilibrium configuration of the structure and the corresponding displacements through the minimization of the total potential energy.

$$\pi = \partial U + \partial V \qquad (10)$$

$$\pi = \left[N_x u_0 + \left(\frac{4}{h}\frac{dM_x}{dx} - \frac{16}{h^3}\frac{dP_x}{dx} + \left(1 - \frac{4}{h} \right) Q_x + \frac{16}{h^3}R_x \right) w_0 + \left(-\frac{4M_x}{h} + \frac{16P_x}{h^3} \right) \frac{dw_0}{dx} + \left(\left(1 - \frac{4}{h} \right) M_x + \left(1 - \frac{4}{h} \right) Q_x + \frac{16}{h^3}(P_x + R_x) \right) \varnothing \right]_0^L + \int_0^L \left[-\frac{dN_x}{dx} u_0 + \left(\left(-\frac{4}{h}\frac{d^2 M_x}{dx^2} + \frac{16}{h^3}\left(\frac{d^2 P_x}{dx^2} - \frac{dR_x}{dx} \right) - \left(1 + \frac{4}{h} \right) \frac{dQ_x}{dx} \right) - q \right) w_0 + \left(-\left(1 + \frac{4}{h} \right) \frac{dM_x}{dx} - \frac{16}{h^3}\frac{dP_x}{dx} \right) \varnothing \right] dx \qquad (11)$$

Specify the boundary conditions and the displacements at the ends of the beam as in Eq. (12).

$$\left\{ \begin{array}{c} u_0 \\ w_0 \\ \frac{dw_0}{dx} \\ \varnothing \end{array} \right\} \quad OR \quad \left\{ \begin{array}{c} N_x \\ \frac{4}{h}\frac{dM_x}{dx} - \frac{16}{h^3}\frac{dP_x}{dx} + \left(1 - \frac{4}{h} \right) Q_x + \frac{16}{h^3}R_x \\ -\frac{4M_x}{h} + \frac{16P_x}{h^3} \\ \left(1 - \frac{4}{h} \right) M_x + \left(1 - \frac{4}{h} \right) Q_x + \frac{16}{h^3}(P_x + R_x) \end{array} \right\} \qquad (12)$$

The equilibrium equations can be expressed as Eqs. (13) - (15)

$$-\frac{dN_x}{dx} = 0 \qquad (13)$$

$$\left(-\frac{4}{h}\frac{d^2 M_x}{dx^2} + \frac{16}{h^3}\left(\frac{d^2 P_x}{dx^2} - \frac{dR_x}{dx} \right) - \left(1 + \frac{4}{h} \right) \frac{dQ_x}{dx} \right) = q \qquad (14)$$

$$\left(1 + \frac{4}{h} \right) \frac{dM_x}{dx} + \frac{16}{h^3}\frac{dP_x}{dx} = 0 \qquad (15)$$

The Eq. (13) states that the rate of change of the axial force N_x indicates equilibrium in the axial direction. While Eq. (14) represents the equilibrium of transverse forces and moments with the applied load, and Eq. (15) represents equilibrium in the bending moment with respect to x. The equilibrium conditions required for buckling analysis are represented by these equations, which offer valuable insights into the forces and moment distribution within the FGPB. They play a vital role in the determination of the critical load at which buckling arises and in the prediction of the structure's behavior under diverse loading conditions. The solution for Eqs. (13)–(15) is obtained using KT conditions. In order to solve the equilibrium equations by employing the KT conditions, it is necessary to initially transform the problem into a restricted optimization paradigm. In the context of restricted optimization problems, the KT conditions are employed to address scenarios where the objective function is bound by inequality restrictions. The equilibrium equations serve as restrictions in this scenario.

Kuhn-Tucker conditions

The KT conditions consist of the following:

Stationarity: The gradient of the Lagrangian with respect to the variables is zero.
Primal feasibility: The primal variables satisfy the original constraints.
Dual feasibility: The Lagrange multipliers associated with the constraints are non-negative.
Complementary slackness: The product of each Lagrange multiplier and its associated constraint must be zero.

In order to implement the KT conditions on the equilibrium equations, it is necessary to construct the Lagrangian. The Lagrangian is obtained by adding the goal function, the total potential energy, to the products of Lagrange multipliers and constraints. Subsequently, the Lagrangian is differentiated with regard to the variables and the Lagrange multipliers, and the resultant equations are assigned a value of zero. The corresponding slackness condition is likewise enforced. After successfully solving the system of equations, the solutions for the variables and Lagrange multipliers would be derived, which serve as indicators of the system's equilibrium state.

Assume that $f_k(x)$ $(k = 0, 1, 2, \cdots . m)$ are all differentiable if the function $f_0(x)$ attains at point x^0 a local minimum subject to the set $K = \left\{ \frac{x}{f_i(x)} \leq 0 (i = 1, 2, 3, \cdots \cdots . m) \right\}$ then there exists a vector of Lagrange multiplier U^0 such that the following conditions are satisfied as shown in Fig. 2.

$$\frac{\partial f_0(x^0)}{\partial x_j} + \sum_{i=1}^{m} U_i^0 \frac{\partial f_0(x^0)}{\partial x_j} = 0 (j = 1, 2, 3, \cdots \cdots , n)$$

$$f_i(x^0) \leq 0 (i = 1, 2, 3, \cdots . m)$$

$$u_i^0 f_i(x^0) = 0 (i = 1, 2, 3, \cdots ., m)$$

$$u_i^0 \geq 0 (i = 1, 2, 3, \cdots . m)$$

These conditions are necessary conditions for a local minimum of problems, for maximization problems, the non-negativity condition $U^0 \leq 0$, are called the KT condition.

$$L(x, y, u) = f_0(x) + \sum_{i=1}^{m} u_i(f_i(x) + y_i^2) \tag{16}$$

The necessary conditions for its local minimum are,

$$\frac{\partial L}{\partial x_j} = \frac{\partial f_0(x^0)}{\partial x_j} + \sum_{i=1}^{m} u_i^0 \frac{\partial \left[f_i(x^0) + (y_i^0)^2 \right]}{\partial x_j} = 0$$

$$\frac{\partial L}{\partial y_i} = 2 u_i^0 y_i^0 = 0 (j = 1, 2, 3, \cdots . n)$$

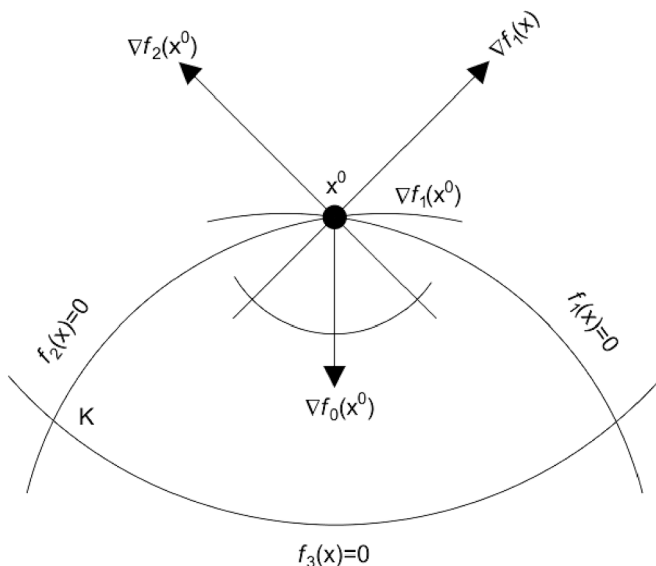$$\frac{\partial L}{\partial u_i} = f_i(x^0) + (y_i^0)^2 = 0 (i = 1, 2, 3, \cdots m)$$

Fig. 2. Kuhn-Tucker condition.

$$\frac{\partial f_0[x^0(b)]}{\partial b_i} = -u_i^0 (i = 1, 2, 3, \cdots . m)$$

Without slack variables, the mathematical problem,

$$L(x, u) = f_0(x) + \sum_{i=1}^{m} u_i f_i(x)$$

The KT condition can be rewritten as,

$$\frac{\partial L(x^0, u^0)}{\partial x_j} = 0 (j = 1, 2, 3, \cdots . n)$$

$$\frac{\partial L(x^0, u^0)}{\partial u_i} \leq 0 (i = 1, 2, 3, \cdots . m)$$

$$u_i^0 \frac{\partial L(x^0, u^0)}{\partial u_i} = 0 (i = 1, 2, 3, \cdots . m)$$

$$u_i^0 \geq 0 (i = 1, 2, 3, \cdots m)$$

If the multiplier u_i is positive, then the corresponding ith constraint is binding (boundary solution). When the function $u_0(x, y)$, $w_0(x, y)$, and $\varnothing_0(x, y)$ are expressed as generalised co-ordinates, it can be represented as Lagrange equations. Kuhn-Tucker condition can be written as follows based on the table values.

$$u_0(x, y) = \sum_{i=1}^{m} f_i(x^0) \theta_i e^{i\lambda y} \tag{17}$$

$$w_0(x, y) = \sum_{i=1}^{m} f_i(x^0) \varphi_i e^{i\lambda y} \tag{18}$$

$$\varnothing_0(x, y) = \sum_{i=1}^{m} f_i(x^0) \psi_i e^{i\lambda y} \tag{19}$$

where, θ_i, φ_i, and ψ_i are the three different boundary conditions and λ is the scalar. Kuhn-Tucker boundary conditions are utilized for mathematical calculations as stated in Table 2.

$$\frac{\partial^2 \pi}{\partial M_j^2} = 0, \frac{\partial^2 \pi}{\partial N_j^2} = 0, \frac{\partial^2 \pi}{\partial P_j^2} = 0 \tag{20}$$

$$\left\{ \begin{bmatrix} F_{11} & F_{12} & F_{13} \\ F_{21} & F_{22} & F_{23} \\ F_{31} & F_{32} & F_{33} \end{bmatrix} - \lambda^2 \begin{bmatrix} 0 & 0 & 0 \\ 0 & R_{22} & 0 \\ 0 & 0 & 0 \end{bmatrix} \right\} \begin{bmatrix} M \\ N \\ P \end{bmatrix} = \begin{bmatrix} 0 \\ 0 \\ 0 \end{bmatrix}$$

$$\left\{ \begin{bmatrix} F_{11} & F_{12} & F_{13} \\ F_{21} & F_{22} & F_{23} \\ F_{31} & F_{32} & F_{33} \end{bmatrix} - \begin{bmatrix} 0 & 0 & 0 \\ 0 & \lambda^2 R_{22} & 0 \\ 0 & 0 & 0 \end{bmatrix} \right\} \begin{bmatrix} M \\ N \\ P \end{bmatrix} = \begin{bmatrix} 0 \\ 0 \\ 0 \end{bmatrix}$$

$$F_{11}(i, j) = M \int_0^L e^{\lambda x(x+1)} \theta_{i,x}, \theta_{j,x} dx$$

$$F_{12}(i, j) = F_{21}(i, j) = P \int_0^L e^{\lambda x(x+1)} \theta_{i,x}, \theta_{j,x} dx$$

$$F_{13}(i, j) = F_{31}(i, j) = (N - \alpha M) \int_0^L e^{\lambda(x+1)} \theta_{i,x}, \varphi_{i,x} dx$$

$$F_{22}(i, j) = \alpha^2 [F_{12}(i, j)][F_{13}(i, j)]$$

Table 2
The boundary conditions based on the KT conditions.

Boundary condition	$x = 0$	$x = L$
SS	$u = 0, w = 0$	$w \leq 0$
CC	$u = 0, w \leq 0, \varnothing = 0, w' \leq 0$	$u = 0, w \leq 0, \varnothing = 0, w' \leq 0$
CF	$u = 0, w = 0, \varnothing = 0, w' = 0$	–

$$F_{23}(i,j) = F_{32}(i,j) = (\beta^2 - \alpha F)[F_{22}(i,j)]$$

$$F_{33}(i,j) = \lambda^2 R_{22} \int_0^L e^{\lambda x(x+1)} \theta_i, \theta_i dx$$

$$R_{11} = R_{12} = R_{13} = R_{21} = R_{23} = R_{31} = R_{32} = R_{33} = 0$$

$$R_{22}(i,j) = (\alpha^2 M - \beta N)[F_{33}(i,j)]$$

where, $i,j = 1, 2, 3, \cdots\cdots n$

The non-dimensional critical buckling $(\overline{N}_{cr})$ of FGPB is estimated using Eq. (21) [51].

$$\overline{N}_{cr} = N_{cr}\frac{12L^2}{E_c h^3} \tag{21}$$

The $\overline{N}_{cr}$ for SS, CC, and CF boundary conditions at different values of gradient index (p_x, $p_z = 0, 0.5, 1, 2, 3, 4, 5, 6, 7, 8, 9,$ and 10), aspect ratio (L/h = 5, 10, 15, 20, 25, 30, and 35), porosity index ($\alpha = 0, 0.1, 0.2, 0.3$) is presented in Appendix as Tables 4–9.

System reliability assessment

Due to the rapid advancement of science and technology and to meet the ever-increasing needs of society, industries are increasingly introducing automation for producing goods ranging from the simplest to highly complex systems. The system reliability of a component, device, equipment, unit, or system is the probability that it performs its intended function adequately for a specified period of time under the given operating conditions. Component failure times vary among identical components operating under similar conditions, making it challenging to predict their exact failure times. Instead, failure can be described in probabilistic terms [52]. The effect of porosity (failure rate) on the beam's structural system reliability under buckling conditions is presented as follows:

Let N_0 identical systems be put into operation at time $t = 0$ under identical conditions. After t units of time,

$$N_s(t) = \text{Number of components that are operating at time } t \tag{22}$$

$$N_f(t) = \text{Number of components that have failed at time } t \tag{23}$$

then system reliability $R(t)$ at time t is defined as,

$$R(t) = \frac{N_s(t)}{N_0} \tag{24}$$

Thus, system reliability of a component/system at time t is the probability that it performs its function without failure. Being a probability, its value lies between 0 and 1. From Eq. (22), if $N_s(t) = 0$, then $R(t) = 0$ and if $N_s(t) = N_0$, then $R(t) = 1$.

By definition, $N_s(t)$ satisfies the following relation:

$0 \leq N_s(t) \leq N_0$ for any time interval $[0, t]$, and
$\frac{0}{N_0} \leq \frac{N_s(t)}{N_0} \leq \frac{N_0}{N_0} \Rightarrow 0 \leq R(t) \leq 1$

System reliability at time, t in the interval $[0, t]$, can be defined as given in Eq. (25).

$$R(t) = \frac{Number of components performing intended funcition at time t}{Number of components at start (i.e., when t = 0)} \tag{25}$$

Mean Time to Failure (MTTF) is computed as the average duration until the initial malfunction of a given system, assembly, or component occurs [53]. The MTTF of a given system can be estimated using Eq. (26)

$$MTTF = \frac{1}{n}\sum_{i=1}^n t_i \tag{26}$$

A sample of 12 experiments is considered, and the time for which each of the 12 components operates successfully is estimated as follows:

$$MTTF = E(T) = \int_0^\infty tf(t)dt = \int_0^\infty t\left(-\frac{d}{dt}R(t)\right)dt \left[\because f(t) = -\frac{d}{dt}R(t)\right]$$

Integrating by parts,

$$MTTF = t(-R(t))_0^\infty - \int_0^\infty (1)(-R(t))dt = [tR(t)]_{t\to\infty} - 0 + \int_0^\infty R(t)dt$$

Since $R(t) = e^{-\int_0^\infty \lambda(t)dt}$ & $\lim_{x\to\infty} x^n e^{-x} = 0$ for $n > -1$

$$MTTF = \int_0^\infty R(t)dt$$

$$MTTF = \frac{1}{\lambda} or \lambda = \frac{1}{MTTF}$$

The reliability range (RR) for the 10 experiments in the system are presented in MTTF plot (Fig. 3) and in Table 3. It can be seen from Fig. 3 that Exp. No. 9, and 11 are eliminated as these experiments are not reliable as per the system reliability range estimation.

The bathtub curve offers valuable insights into the temporal patterns of failure exhibited by FGPB structures. Understanding factors contributing to increased failure probability is crucial for improving structure dependability and establishing efficient maintenance methodologies. As no component is perfect and cannot last forever, after the span of useful life, the failure rate of the system starts increasing due to the aging of the system in the phase of decreasing failure rates [54], as shown in the bathtub curve (Fig. 4). These first failures are often attributed to design, manufacturing, or testing errors. In this phase, the failure rate is high, but it decreases as faulty components are found and replaced. The curve's center represents the phase of almost constant failure rate, which has a low failure rate. The system is considered operationally sturdy and unlikely to fail. The system's dependability throughout the experiments depends on proper maintenance and operation. Late in the system's life cycle, phase of increasing failure rate occurs. Due to gradient index, aspect ratio, porosity index, and other factors, the system may function poorly. In this phase, the failure rate rises, suggesting that the system is reaching its end and that the aging mechanisms cause wear-out failures, reducing system reliability.

Results and discussion

In this study, to estimate the system reliability and section reliability for mechanical systems, the *k-out of-n* system is adapted. The reliabilities are calculated using the Evolutionary method, GRG Non-linear, and Lagrangian methods in the Excel solver. Evolutionary methods are
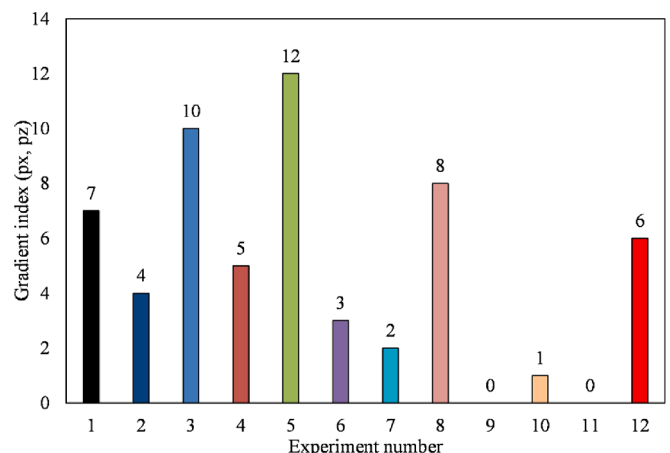

Fig. 3. MTTF plot.

Table 3
The estimations of reliability range and gradient index for the experiments.

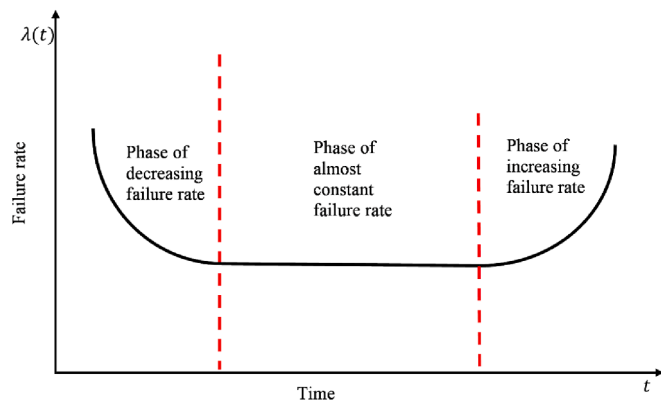| Exp. No.	Gradient Index (P_x, P_z)	Reliability range
1	0	7
2	0.5	4
3	1	10
4	2	5
5	3	12
6	4	3
7	5	2
8	6	8
9	7	0
10	8	1
11	9	0
12	10	6

Fig. 4. Bathtub curve.

useful for complex systems where analytical solutions may be difficult or unattainable [55]. They can handle uncertainties and nonlinearities and explore a large solution space. Evolutionary algorithms could solve reliability engineering challenges like FGBs and buckling behaviour due to their flexibility. The GRG Non-linear method is advantageous for its ability to handle complex, nonlinear and non-convex optimization problems [56]. Its application in reliability analysis allows for the efficient exploration of the design space to identify solutions that satisfy reliability requirements. The Lagrangian method is employed in the FGPB structural and reliability analysis, as this method is particularly useful when dealing with constrained optimization problems where both reliability requirements and design constraints need to be satisfied simultaneously [57]. Tables 4–9 (Appendix) present the non-dimensional critical buckling at gradient index (0, 0.5, 1, 2, 3, 4, 5, 6, 7, 8, 9, and 10), aspect ratio (5, 10, 15, 20, 25, 30, and 35), porosity index (0, 0.1, and 0.2) and boundary conditions (simply supported, clamped–clamped, and clamped-free).

The effect of aspect ratio on non-dimensional critical buckling

$\overline{N}_{cr}$ is significantly influenced by the aspect ratio across all boundary conditions for the fixed gradient index in both directions. It is observed from Tables 4–6 that for an SS boundary condition, at $P_x = 0$ and $P_z = 0$ the values of $\overline{N}_{cr}$ at L/h = 5, 10, 15, 20, 25, 30 and 35 were found to be 54.174, 56.761, 59.349, 61.937, 63.231, 63.878 and 64.202, respectively. Whereas, for CC boundary condition, at $P_x = 0$, $P_z = 0$, the values of $\overline{N}_{cr}$ at L/h = 5, 10, 15, 20, 25, 30 and 35 were found to be 184.239, 193.376, 202.514, 211.651, 216.220, 218.504, and 219.646, respectively. However, for the CF boundary condition, at $P_x = 0$, $P_z = 0$, the values of $\overline{N}_{cr}$ at L/h = 5, 10, 15, 20, 25, 30 and 35 were found to be 12.937, 13.579, 14.221, 14.862, 15.183, 15.343, 15.424, respectively. This highlights the significance of gradient index, boundary conditions

and aspect ratio in determining the $\overline{N}_{cr}$ of FGPBs. In the case of SS boundary conditions, the values of $\overline{N}_{cr}$ exhibit a consistent upward trend as the aspect ratio increases. This observation implies that there is a positive correlation between the length of the beam in relation to its thickness and the critical buckling stress, suggesting enhanced stability. The impact of the gradient index and material qualities on the rate of growth in $\overline{N}_{cr}$ with increasing aspect ratio may exhibit variability. In contrast, the critical buckling load values for CC boundary conditions exhibit a notable increase in comparison to SS boundary conditions. This observation suggests that the beam exhibits more stability when securely fastened at both ends, leading to an increased ability to withstand buckling forces [21]. The $\overline{N}_{cr}$ values for CF boundary conditions are significantly lower in comparison to SS and CC boundary conditions. This suggests that the stability of the beam decreases when one end is clamped while the other is free, leading to a reduced ability to withstand buckling [28]. Irrespective of the boundary conditions, an increase in the aspect ratio often leads to a rise in the critical buckling load. These findings indicate that beams with greater length in relation to their thickness have increased resistance to buckling, which aligns with the principles of HSDT. Furthermore, it is crucial to take into account both aspect ratio and boundary conditions while designing and analyzing FGPBs in order to guarantee their structural stability and integrity.

The effect of gradient index on non-dimensional critical buckling

$\overline{N}_{cr}$ is significantly influenced by the gradient index on both directions at the fixed aspect ratio across all boundary conditions. It is observed from Tables 4–6 that under the SS boundary condition, at the considered gradient index in the *x*-direction $P_x = 5$ and aspect ratio L/h = 20, the values of $\overline{N}_{cr}$ at $P_z = 0$, 5 and 10 were found to be 25.147, 16.510 and 15.727, respectively. Whereas, under the CC boundary condition, at the considered gradient index in *x*-direction $P_x = 5$ and aspect ratio L/h = 20, the values of $\overline{N}_{cr}$ at $P_z = 0$, 5 and 10 were found to be 86.302, 60.678 and 58.750, respectively. However, under the CF boundary condition, at the considered gradient index in *x*-direction $P_x = 5$ and aspect ratio L/h = 20, the values of $\overline{N}_{cr}$ at $P_z = 0$, 5 and 10 were found to be 6.060, 4.261 and 4.125, respectively. As the P_z increases, the $\overline{N}_{cr}$ decreases for all boundary conditions, and this observation suggests that an increase in the gradient of the material in the *z*-direction results in less structural stability and decreased resistance to buckling [32]. The observed decline in $\overline{N}_{cr}$ as P_z increases implies that beams exhibiting more pronounced alterations in material characteristics along the *z*-direction are more susceptible to buckling. The $\overline{N}_{cr}$ exhibits the largest value for any given Pz value under CC boundary conditions, respectively, followed by SS and CF boundary conditions, which highlights the impact of boundary conditions on the beam's structural stabiligy. [48]. CC beams offer enhanced support and stability, leading to increased critical buckling loads in comparison to circumstances where the ends are SS and CF. The observed changes in $\overline{N}_{cr}$ as a function of Pz underscore the importance of material gradient profiles in determining beam stability. These findings indicate that the optimization of buckling behavior and structural stability in FGPBs is contingent upon the management of the gradient index in the *z*-direction [51]. Furthermore, the significant variations in $\overline{N}_{cr}$ across various boundary conditions underscore the significance of carefully choosing suitable boundary conditions that align with the unique demands and loading circumstances of the given application. The relationship between the $\overline{N}_{cr}$ and the gradient index in the *z*-direction is inversely proportional. Elevated levels of P_z result in diminished $\overline{N}_{cr}$ values, hence suggesting a decrease in structural integrity. In comparison to beams with steeper gradients, beams characterized by more gradual changes in material characteristics in the *z*-direction have enhanced resistance to buckling.

For the fixed gradient in the z-direction, $P_z = 5$ and aspect ratio L/h = 20, under SS boundary condition, the values of $\overline{N}_{cr}$ at $P_x = 0$, 5 and 10

were found to be 61.937, 27.458 and 19.453, respectively. Whereas, under the CC boundary condition, at the considered gradient index in z-direction $P_z = 5$ and aspect ratio $L/h = 20$, the values of $\overline{N}_{cr}$ at $P_x = 0$, 5 and 10 were found to be 211.651, 86.302 and 76.233, respectively. However, under the CF boundary condition, at the considered gradient index in z-direction $P_z = 5$ and aspect ratio $L/h = 20$, the values of $\overline{N}_{cr}$ at $P_x = 0$, 5 and 10 were found to be 14.862, 6.060 and 5.353, respectively. The $\overline{N}_{cr}$ experiences a notable reduction when the Px is increased, regardless of the boundary conditions. This implies that beams exhibiting more pronounced heterogeneity in material qualities along the *x*-axis are more susceptible to buckling in comparison to beams with more gradual fluctuations [32]. From a physical point of view, a greater gradient index in the *x*-direction signifies a more sudden shift between materials, leading to increased stress concentrations and less structural stability [48]. The CC exhibits the highest $\overline{N}_{cr}$ values followed by the SS and CF conditions, similar to the preceding case. In comparison to SS and CF conditions, the CC beam offers enhanced support and resistance to buckling, leading to increased critical buckling stresses [51]. The significance of meticulously tailoring the material gradient profiles, especially in the *x*-direction, to augment the structural stability of FGPBs is emphasized, and the buckling behavior is substantially influenced by the selection of boundary conditions.

System reliability assessment based on aspect ratio for SS, CC, and CF boundary conditions

It can be seen from Table 10 that for exponential (0, 5), the variance of gradient index using Evolutionary, GRG Non-linear, and Lagrangian is estimated to be 25.04 %, 25.04 %, and 24.00 %, respectively. While the exponential is estimated to be 0.74, 0.75, and 0.74. The variances for the gradient index estimates using Evolutionary, GRG Non-linear, and Lagrangian methods are relatively close in both scenarios. This suggests a certain level of consistency across the methods in estimating the gradient index for the given distributions. The small differences may be attributed to the inherent characteristics and numerical behavior of each method [33]. Whereas, for exponential (6, 10), the variance of the gradient index is estimated to be 75.02 %, 74.62 %, and 74.52 %, respectively. The higher variance for exponential (6, 10) suggests that

the system reliability analysis becomes more sensitive to variations in the system parameters when the distribution parameters are higher. Coit and Zio [58] suggest that higher variability might be expected in situations where failure rates are higher, or the system is more prone to failure. Notably, in both scenarios, the Lagrangian method shows a slightly lower variance compared to the Evolutionary and GRG Non-linear methods. This could indicate that the Lagrangian method is more robust or less sensitive to parameter variations in these specific scenarios [59]. As estimated by the evolutionary algorithm, the variance of system parameters such as aspect ratio and gradient index reflects the design's sensitivity to variations in input parameters and model assumptions. Indicating increased uncertainty and variability in the response of the system, higher variance values draw attention to possible domains that require additional optimization and refinement. In a similar trend, the variance derived from the GRG non-linear method offers valuable insights regarding the degree to which system parameters are susceptible to variations in design variables and constraints. By examining trends in variance across various scenarios, it is possible to discern crucial parameters that influence the behavior and dependability of a system. The variance computed utilizing the Lagrangian optimization method provides significant insights into the structural design's resilience and constancy. A reduced variance implies enhanced consistency and dependability in the estimation of system parameters, signifying a system response that is more stable and predictable.

On the other hand, for exponential (0, 5), the variance of aspect ratio using Evolutionary, GRG Non-linear, and Lagrangian is estimated to be 20.59 %, 19.06 %, and 20.05 %, respectively. The exponential is estimated to be 0.72, 0.71, and 0.72. The variances for the aspect ratio estimates using the Evolutionary and Lagrangian methods are similar in both scenarios, with the Lagrangian method showing a slightly lower variance. This indicates that, for the given distribution parameters, these two methods perform comparably in estimating the aspect ratio. Whereas, for exponential (6, 10), the variance of aspect ratio is estimated to be 75.34 %, 74.54 %, and 74.65 %, respectively. The higher variances observed for the exponential (6, 10) scenario compared to the exponential (0, 5) scenario suggest that the aspect ratio is more sensitive to variations and complexities in the system under the second set of distribution parameters [60]. It can be inferred from Table 10 that the

Table 10
System reliability model for non-dimensional critical buckling at various aspect ratios and gradient index.

System reliability- aspect ratio				
Boundary conditions	⟶	SS, CC, CF	SS, CC, CF	SS, CC, CF
Reliability methods	Methods	Evolutionary	GRG Non-linear	Lagrangian
	Polynomial	0.89	0.89	0.8
	Exponential	0.53	0.53	0.78
For exponential (0, 5)	Variance of gradient index	25.04%	25.04%	24.00%
	Variance of aspect ratio	20.59%	19.06%	20. 05%
	Exponential	0.74	0.75	0.74
For exponential (6, 10)	Variance of gradient index	75.02%	74.62%	74.52%
	Variance of aspect ratio	75.34%	74.54%	74.65%
	Exponential	0.72	0.71	0.72
Result			10-out of-12 system is reliable	

10 out of 12 system is reliable.

System reliability assessment based on even porosity for SS, CC, and CF boundary conditions

Table 11 presents the results of system reliability for FGPB under SS, CC, and CF boundary conditions under even porosity, adapting Evolutionary, GRG Non-linear, and Lagrangian methods. It can be seen from Table 11 that for exponential (0, 0.1), the variance of porosity index using Evolutionary, GRG Non-linear, and Lagrangian methods is found to be 28.14 %, 25.79 %, and 57.00 %, respectively. Whereas, for exponential (0.1, 0.2), the variance of porosity index using Evolutionary, GRG Non-linear, and Lagrangian methods is found to be 85.78 %, 74.32 %, and 61.62 %, respectively. The exponential is found to be 0.74, 0.75, and 0.74. The results indicate that the porosity index estimates are highly sensitive to changes in the distribution parameters, with consistent ordering of variances among the three methods. Across both scenarios, the ordering of variances among the three methods remains consistent: GRG Non-linear < Lagrangian < Evolutionary. GRG Non-linear consistently exhibits the lowest variance, while the Lagrangian method consistently has the highest variance. This may suggest that the Lagrangian method is more sensitive or less stable in estimating the porosity index, especially when dealing with specific distribution parameters [61]. The larger variances in the exponential (0.1, 0.2) may indicate increased complexity or variability in the system. The substantial rise in variances observed for both porosity and gradient index estimates during the transition from exponential (0, 0.1) to exponential (0.1, 0.2) distributions underscores the importance of employing resilient optimization techniques to deal with the uncertainties and complexity of the system. As the primary objective of design optimization endeavours to minimize the impact of distribution parameters on performance and dependability, the Lagrangian method consistently achieves the lowest variance when estimating the gradient index, indicating its potential applicability in scenarios where stability and robustness are critical.

On the other hand, for exponential (0, 0.1), the variance of gradient index using Evolutionary, GRG Non-linear, and Lagrangian methods is found to be 28.59 %, 29.06 %, and 28.07 %, respectively. Whereas, for exponential (0.1, 0.2), the variance of gradient index using Evolutionary, GRG Non-linear, and Lagrangian methods is found to be 87.12 %, 84.54 %, and 82.15 %, respectively. The exponential is found to be 0.76, 0.75, and 0.76. The variances of the gradient index estimates are significantly influenced by changes in the distribution parameters. The transition from exponential (0, 0.1) to exponential (0.1, 0.2) results in a substantial increase in variances for all three methods. This suggests that the gradient index is highly sensitive to variations in the mean and standard deviation of the exponential distribution. Across both scenarios, the ordering of variances among the three methods remains consistent: Lagrangian < Evolutionary < GRG Non-linear. Lagrangian consistently exhibits the lowest variance, indicating higher stability or robustness in estimating the gradient index, while GRG Non-linear consistently has the highest variance [62]. It can be inferred from Table 11 that the 10 out of 12 system is reliable based on the performance criteria given in terms of boundary conditions and distribution parameters. This instils assurance in the structural design and indicates that the optimized configurations possess the strength to endure expected loads and environmental circumstances.

System reliability assessment based on uneven porosity for SS, CC, and CF boundary conditions

Table 12 presents the system reliability results of buckling analysis of an FGPB for SS, CC, and CF boundary conditions for uneven porosity distribution. It can be seen from Table 12 that for exponential (0, 0.1), the variance of porosity index using Evolutionary, GRG Non-linear, and Lagrangian is estimated to be 18.14 %, 15.18 %, and 17.00 %, respectively. Whereas, for exponential (0.1, 0.2), the variance of porosity index using Evolutionary, GRG Non-linear, and Lagrangian is estimated to be 55.19 %, 44.12 %, and 51.00 %, respectively. The exponential is found to be 0.44, 0.35, and 0.34. The transition from exponential (0, 0.1) to exponential (0.1, 0.2) results in an increase in variances for all three methods, which indicates that the porosity index is sensitive to variations. Across both scenarios, the ordering of variances among the three methods remains consistent: GRG Non-linear < Lagrangian < Evolutionary. GRG Non-linear consistently exhibits the lowest variance, while the Evolutionary method consistently has the highest variance. The GRG

Table 11
System reliability model for even porosity.

System reliability- porosity (even)				
Boundary conditions →		SS, CC, CF	SS, CC, CF	SS, CC, CF
Reliability methods	Methods	Evolutionary	GRG Non-linear	Lagrangian
	Polynomial	0.56	0.56	0.5
	Exponential	0.46	0.47	0.7
For exponential (0, 0.1)	Variance of porosity index	28.14%	25.79%	57%
	Variance of gradient index	28.59%	29.06%	28. 07%
	Exponential	0.74	0.75	0.74
For exponential (0.1, 0.2)	Variance of porosity index	85.78%	74.32%	61.62%
	Variance of gradient index	87.12%	84.54%	82.15%
	Exponential	0.76	0.75	0.76
Result			10-out of-12 system is reliable	

Table 12
System reliability model for uneven porosity.

System reliability- porosity (uneven)				
Boundary conditions		SS, CC, CF	SS, CC, CF	SS, CC, CF
Reliability methods	Methods	Evolutionary	GRG Non-linear	Lagrangian
	Polynomial	0.36	0.26	0.6
	Exponential	0.26	0.27	0.5
For exponential (0, 0.1)	Variance of porosity index	18.14%	15.18%	17%
	Variance of gradient index	18.59%	18.00%	8. 07%
	Exponential	0.44	0.35	0.34
For exponential (0.1, 0.2)	Variance of porosity index	55.19%	44.12%	51%
	Variance of gradient index	45.19%	34.12%	61%
	Exponential	0.34	0.44	0.40
Result		System is not reliable		

Non-linear method consistently shows the lowest variance among the three methods, indicating higher stability or robustness in estimating the porosity index. This method may be more reliable in providing consistent results under different distribution parameters for this specific application.

On the other hand, for exponential (0, 0.1), the variance of gradient index using Evolutionary, GRG Non-linear, and Lagrangian is estimated to be 18.59 %, 18.00 %, and 8.07 %, respectively. Whereas, for exponential (0.1, 0.2), the variance of gradient index using Evolutionary, GRG Non-linear, and Lagrangian is estimated to be 45.19 %, 34.12 %, and 61.00 %, respectively. The exponential is estimated to be 0.34, 0.44, and 0.40, respectively. Across both scenarios, the ordering of variances among the three methods remains consistent: Lagrangian < Evolutionary < GRG Non-linear. Lagrangian consistently exhibits the lowest variance, while GRG Non-linear consistently has the highest variance. The Lagrangian method consistently shows the lowest variance among the three methods, indicating higher stability or robustness in estimating the gradient index. The differences in variances highlight potential trade-offs between methods, and the choice of method may depend on the specific characteristics of the system under consideration. It can be inferred from Table 12 that the system is not reliable.

Utilized assumptions and limitations

The reliability analysis executed in the present study is based on the assumptions that the FGPB exhibits linear elastic behaviour when subjected to loading conditions, which simplifies the analysis, perhaps limiting its ability to effectively represent the behaviour of FGPBs subjected to significant deformations or nonlinear loading conditions. The study potentially overlooks dynamic loading or transitory impacts by assuming static loading conditions only. Dynamic loading circumstances may provide distinct issues and necessitate supplementary considerations, notwithstanding the useful insights offered by static analysis. The study assumes of a homogeneous distribution of porosity throughout the beams, disregarding any variations or gradients in porosity that may arise during the manufacturing process or because of material deterioration over time. The study of the FGPBs assumes of a uniform change in gradient index, disregarding any differences or discontinuities in material composition that may impact the structural response. To maintain simplicity, the analysis also assumes of isotropic material properties while dismissing the possibility of anisotropic behaviour resulting from factors such as material alignment, fibre orientation, or manufacturing procedures.

The reliability analysis of the FGPB has some potential limitations. Simulating the behaviour of the FGPB and reliability analysis could include the utilization of simplified mathematical models, but these simplifications may fail to consider some intricacies or nonlinearities that exist in real-world situations. The buckling behaviour of beams in practical applications can be influenced by several factors, such as non-uniform loading, transient loads, or dynamic vibrations. The study considers a homogeneous border circumstance, so disregarding the impact of localized boundary effects such as supports, joints, or interface interactions and temperature. The presence of these boundary conditions has the potential to exert a substantial influence on the buckling characteristics of the beams in practical scenarios.

Conclusion

The study used higher-order shear deformation theory to simulate functionally graded porous beams with uniform and non-uniform porosity distributions. The material characteristics were characterized using power law equations. The behaviour of the beams was examined using displacement field and equilibrium equations. Critical buckling loads were calculated for various boundary conditions and gradient index profiles. The system's dependability was evaluated using *k-out-of-n system* reliability analysis:

- The findings highlight the significant impact of changing gradient index and boundary conditions on the buckling characteristics of functionally graded porous beams.
- CC beams provide improved stability and support, resulting in greater critical buckling stresses when compared to SS and CF beams.
- For fixed gradient index values in *x* and *z* directions ($P_x = 5$, $P_z = 5$), the rate of increase in non-dimensional critical buckling for the SS beam is 34.8, 10.9, 8.6, 26.3, 2.7 and 1.1 % at aspect ratios of 5, 10, 15, 20, 25, 30 and 35, respectively. Whereas, for CC beams, it is 49.9,

14.5, 4.2, 24.2, 2.6 and 1.2 %, respectively, and 34.2, 12.8, 4.1, 24.1, 2.6 and 1.3 %, respectively for CF beams.

- For fixed gradient index in the x-direction ($P_x = 8$) and aspect ratio (L/h = 15), the rate of decrease in non-dimensional critical buckling for the SS beam at $P_z = 0$, 5 and 10 are 16.3 % and 16.7 %. Whereas for the CC beam, it is 17.1 % and 16.5 % and for the CF beam, it is 16.8 % and 16.2 %.
- For a fixed gradient in the z-direction (Pz = 5) and aspect ratio (L/h = 20), the rate of decrease in non-dimensional critical buckling for the SS beam at Px = 0, 5 and 10 is 40.1 and 7.9 %, respectively. Whereas, for the CC beam, it is 28.7 % and 2.7 % and for the CF beam, it is 27.5 % and 2.7 %.
- The Lagrangian method consistently demonstrated superior stability and system reliability, yielding lower variances in both gradient and porosity indices compared to Evolutionary and GRG Non-linear methods. This suggests that the Lagrangian method is well-suited for providing reliable estimates of system performance, particularly in scenarios with varying levels of complexity.
- The observed consistent ordering of variances across distribution parameters underscores the trade-offs and considerations involved in selecting an appropriate system reliability analysis method. While the GRG Non-linear method exhibited higher sensitivity, the Lagrangian method emerged as a robust choice, offering consistent and stable results across different scenarios.

This research emphasizes the importance of methodological choices in system reliability analysis and advocates for careful selection based on the specific characteristics of the system under investigation. The Lagrangian method, with its demonstrated stability, stands out as a promising avenue for advancing the field of system reliability analysis in FGPBs and related structural systems. The study offers insights for designing and optimizing structural components from FGPBs, assessing reliability and evaluating dependability in unpredictable environments. It applies to various sectors, emphasizing the importance of structural dependability and functionality.

CRediT authorship contribution statement

Ravikiran Chintalapudi: Writing – original draft, Methodology, Investigation, Formal analysis. **Geetha Narayanan Kannaiyan:** Writing – original draft, Visualization, Formal analysis, Conceptualization. **Bridjesh Pappula:** Validation, Resources, Investigation. **Seshibe Makgato:** Writing – review & editing, Formal analysis.

Declaration of competing interest

The authors declare that they have no known competing financial interests or personal relationships that could have appeared to influence the work reported in this paper.

Data availability

No data was used for the research described in the article.

Appendix

Table 4
$\overline{N}_{cr}$ for SS beam at various aspect ratios.

Exp. No.	P_x; P_z	L/h = 5			L/h = 10			L/h = 15			L/h = 20			L/h = 25			L/h = 30			L/h = 35		
		0	5	10	0	5	10	0	5	10	0	5	10	0	5	10	0	5	10	0	5	10
1	0	54.174	19.656	16.050	56.761	35.468	17.723	59.349	37.557	19.396	61.937	27.585	21.069	63.231	40.690	21.906	63.878	41.212	22.324	64.202	41.474	22.534
2	0.5	39.588	16.687	14.372	41.742	27.551	15.726	43.895	29.269	17.080	46.049	21.801	18.434	47.125	31.753	19.111	47.664	32.274	19.450	47.933	32.489	19.619
3	1	32.282	15.149	13.439	34.215	23.610	14.772	36.148	25.216	16.106	38.081	19.242	17.439	39.048	27.534	18.106	39.531	28.026	18.439	39.773	28.227	18.606
4	2	24.976	13.578	12.454	26.689	19.640	13.767	28.401	21.135	15.079	30.114	17.579	16.392	30.971	23.587	17.648	31.399	24.241	18.277	31.613	24.510	18.591
5	3	22.540	12.654	11.821	24.180	18.268	13.342	25.819	19.843	14.862	27.458	17.020	16.383	28.278	22.101	17.143	28.688	22.598	17.523	28.893	22.795	17.714
6	4	20.105	12.324	11.636	22.338	17.267	13.042	24.570	19.049	14.449	26.803	16.462	15.855	27.919	21.626	16.558	28.477	22.168	16.910	28.756	22.390	17.086
7	5	17.670	11.995	11.450	20.162	16.170	12.843	22.655	17.935	14.335	25.147	16.510	15.727	26.393	20.860	16.423	27.016	21.428	16.771	27.328	21.665	16.945
8	6	17.005	11.687	11.318	19.598	15.862	12.749	22.191	17.322	14.181	24.784	16.423	15.613	26.080	20.663	16.329	26.728	21.251	16.687	27.052	21.496	16.866
9	7	16.341	11.583	11.235	18.825	15.432	12.605	21.308	17.308	13.974	23.792	16.238	15.344	25.034	20.029	16.029	25.654	20.591	16.372	25.965	20.826	16.543
10	8	15.677	11.479	11.151	17.824	14.925	12.509	19.971	16.641	13.866	22.118	15.866	15.223	23.192	19.123	15.902	23.729	19.645	16.241	23.997	19.859	16.411
11	9	15.013	11.375	11.068	16.937	14.456	12.388	18.861	16.051	13.708	20.786	15.537	15.029	21.748	18.353	15.689	22.229	18.841	16.019	22.469	19.041	16.184
12	10	14.349	11.271	10.985	16.050	13.987	12.268	17.751	15.460	13.551	19.453	15.208	14.834	20.304	17.582	15.475	20.729	18.038	15.796	20.942	18.222	15.956

Table 5
$\overline{N}_{cr}$ for CC beam at various aspect ratios.

Exp. No.	P_x; P_z	L/h = 5			L/h = 10			L/h = 15			L/h = 20			L/h = 25			L/h = 30			L/h = 35		
		0	5	10	0	5	10	0	5	10	0	5	10	0	5	10	0	5	10	0	5	10
1	0	184.239	57.834	53.874	193.376	121.702	61.973	202.514	130.273	70.072	211.651	85.194	78.172	216.220	143.130	82.221	218.504	145.273	84.246	219.646	146.344	85.259
2	0.5	111.610	46.904	42.900	120.163	82.408	50.946	128.717	90.686	58.993	137.270	71.051	67.040	141.547	103.101	71.063	143.686	105.170	73.074	144.755	106.205	74.080
3	1	89.650	42.289	38.499	98.027	69.906	46.472	106.404	78.063	54.445	114.781	66.310	62.418	118.970	90.298	66.405	121.064	92.337	68.398	122.111	93.357	69.395
4	2	75.298	39.191	36.428	83.560	62.191	44.383	91.821	70.285	52.338	100.083	63.130	60.292	104.214	82.426	64.269	106.279	84.449	66.258	107.312	85.461	67.252
5	3	70.812	38.395	35.927	79.038	59.859	43.877	87.263	67.935	51.828	95.489	62.313	59.778	99.602	80.048	63.753	101.658	82.067	65.741	102.686	83.076	66.735
6	4	66.327	37.599	35.427	74.517	57.529	43.373	82.707	65.586	51.318	90.896	61.495	59.264	94.991	77.670	63.237	97.038	79.684	65.223	98.062	80.692	66.216
7	5	61.842	36.803	34.926	69.995	55.198	42.867	78.148	63.236	50.809	86.302	60.678	58.750	90.379	75.292	62.720	92.417	77.302	64.706	93.436	78.306	65.698
8	6	59.875	36.483	34.731	68.013	54.190	42.670	76.150	62.219	50.610	84.288	60.349	58.549	88.357	74.263	62.519	90.392	76.271	64.504	91.409	77.275	65.496
9	7	59.169	36.400	34.687	67.301	53.842	42.626	75.433	61.868	50.565	83.565	60.264	58.503	87.631	73.908	62.473	89.664	75.915	64.458	90.680	76.918	65.450
10	8	55.943	35.842	34.339	64.049	52.172	42.275	72.155	60.185	50.210	80.261	59.690	58.146	84.314	72.205	62.114	86.340	74.208	64.098	87.354	75.210	65.090
11	9	53.976	35.520	34.143	62.067	51.163	42.077	70.157	59.168	50.011	78.247	59.361	57.945	82.292	71.176	61.912	84.315	73.177	63.896	85.326	74.178	64.888
12	10	52.010	35.199	33.946	60.084	50.154	41.879	68.159	58.151	49.811	76.233	59.030	57.743	80.271	70.146	61.709	82.289	72.145	63.692	83.299	73.145	64.684

Table 6

$\overline{N}_{cr}$ for CF beam at various aspect ratios.

Exp. No.	P_x & P_z	L/h = 5			L/h = 10			L/h = 15			L/h = 20			L/h = 25			L/h = 30			L/h = 35		
		0	5	10	0	5	10	0	5	10	0	5	10	0	5	10	0	5	10	0	5	10
1	0	12.937	4.061	3.783	13.579	10.200	4.352	14.221	9.148	4.921	14.862	5.882	5.489	15.183	10.051	5.774	15.343	10.201	5.916	15.424	10.276	5.987
2	0.5	7.837	3.294	3.012	8.438	6.488	3.577	9.039	6.368	4.143	9.639	4.989	4.708	9.939	7.240	4.990	10.090	7.385	5.131	10.165	7.458	5.202
3	1	6.295	2.970	2.703	6.883	5.341	3.263	7.472	5.482	3.823	8.060	4.656	4.383	8.354	6.341	4.663	8.501	6.484	4.803	8.575	6.556	4.873
4	2	5.287	2.752	2.558	5.868	4.609	3.117	6.448	4.935	3.675	7.028	4.433	4.234	7.318	5.788	4.513	7.463	5.930	4.653	7.535	6.001	4.722
5	3	4.972	2.696	2.523	5.550	4.384	3.081	6.128	4.770	3.639	6.705	4.376	4.198	6.994	5.621	4.477	7.138	5.763	4.616	7.211	5.834	4.686
6	4	4.658	2.640	2.488	5.233	4.159	3.046	5.808	4.605	3.604	6.383	4.318	4.162	6.670	5.454	4.441	6.814	5.595	4.580	6.886	5.666	4.650
7	5	4.343	2.584	2.453	4.915	3.933	3.010	5.488	4.440	3.568	6.060	4.261	4.125	6.346	5.287	4.404	6.490	5.428	4.544	6.561	5.499	4.613
8	6	4.204	2.562	2.439	4.776	3.835	2.996	5.347	4.369	3.554	5.919	4.238	4.111	6.204	5.215	4.390	6.347	5.356	4.529	6.419	5.426	4.599
9	7	4.155	2.556	2.436	4.726	3.801	2.993	5.297	4.344	3.551	5.868	4.232	4.108	6.153	5.190	4.387	6.296	5.331	4.526	6.368	5.401	4.596
10	8	3.928	2.517	2.411	4.498	3.639	2.969	5.067	4.226	3.526	5.636	4.191	4.083	5.921	5.070	4.362	6.063	5.211	4.501	6.134	5.281	4.571
11	9	3.790	2.494	2.398	4.358	3.541	2.955	4.926	4.155	3.512	5.495	4.168	4.069	5.779	4.998	4.348	5.921	5.139	4.487	5.992	5.209	4.556
12	10	3.652	2.472	2.384	4.219	3.442	2.941	4.786	4.083	3.498	5.353	4.145	4.055	5.637	4.926	4.333	5.778	5.066	4.473	5.849	5.136	4.542

Table 7

$\overline{N}_{cr}$ for SS beam under even and uneven porosity conditions.

Porosity Index	P_x & P_z	Even Porosity							Uneven Porosity						
		0	0.05	0.1	0.15	0.2	0.25	0.3	0	0.05	0.1	0.15	0.2	0.25	0.3
$\alpha = 0$	0	53.088	50.639	48.285	45.982	43.731	41.531	39.383	62.113	59.247	56.493	53.799	51.165	48.591	46.078
	3	16.813	15.094	13.436	11.845	10.302	8.799	7.344	19.671	17.660	15.720	13.859	12.053	10.295	8.593
	10	13.824	12.132	10.001	8.734	6.433	4.867	3.040	16.174	14.137	11.702	9.127	7.527	5.983	3.557
$\alpha = 0.1$	0	48.262	46.035	43.895	41.802	39.755	37.755	35.802	56.466	53.861	51.357	48.908	46.514	44.174	41.889
	3	15.285	13.721	12.215	10.769	9.365	7.999	6.677	17.883	16.054	14.291	12.599	10.958	9.359	7.812
	10	12.567	11.029	9.092	7.940	5.849	4.425	2.764	14.703	12.852	10.638	8.297	6.843	5.440	3.234
$\alpha = 0.2$	0	37.125	35.412	33.766	32.155	30.581	29.043	27.540	43.436	41.432	39.506	37.622	35.780	33.980	32.222
	3	11.757	10.555	9.396	8.283	7.204	6.153	5.136	13.756	12.349	10.993	9.692	8.429	7.199	6.009
	10	9.667	8.484	6.994	6.108	4.499	3.404	2.126	11.310	9.886	8.183	6.383	5.264	4.184	2.488

Table 8

$\overline{N}_{cr}$ for CC beam under even and uneven porosity conditions.

Porosity Index	P_x & P_z	Even Porosity							Uneven Porosity						
		0	0.05	0.1	0.15	0.2	0.25	0.3	0	0.05	0.1	0.15	0.2	0.25	0.3
$\alpha = 0$	0	183.295	176.293	168.059	160.007	152.134	144.442	136.929	214.455	206.262	196.630	187.208	177.997	168.997	160.207
	3	43.792	38.771	33.930	27.347	20.973	14.196	7.650	51.237	45.363	39.698	31.996	24.538	16.609	8.950
	10	36.565	29.452	25.640	17.873	12.063	7.564	2.869	42.782	36.133	29.999	19.635	14.576	9.224	3.357
$\alpha = 0.1$	0	166.632	160.266	152.781	145.461	138.304	131.310	124.481	194.959	187.511	178.754	170.189	161.815	153.633	145.643
	3	39.811	35.247	30.846	24.861	19.066	12.905	6.954	46.579	41.239	36.089	29.087	22.307	15.099	8.136
	10	33.241	26.775	23.310	16.249	10.966	6.876	2.609	38.892	32.848	27.272	17.850	13.251	8.385	3.052
$\alpha = 0.2$	0	128.178	123.282	117.524	111.893	106.387	101.008	95.755	149.969	144.239	137.503	130.915	124.473	118.179	112.033
	3	30.624	27.113	23.727	19.124	14.666	9.927	5.349	35.830	31.722	27.761	22.375	17.159	11.615	6.259
	10	25.570	20.596	17.930	12.499	8.436	5.289	2.007	29.917	25.268	20.979	13.731	10.193	6.450	2.348

Table 9

$\overline{N}_{cr}$ for CF beam under even and uneven porosity conditions.

Porosity Index	P_x & P_z	Even Porosity							Uneven Porosity						
		0	0.05	0.1	0.15	0.2	0.25	0.3	0	0.05	0.1	0.15	0.2	0.25	0.3
$\alpha = 0$	0	21.679	20.696	19.751	18.826	17.922	17.038	16.175	25.364	24.214	23.108	22.027	20.969	19.935	18.925
	3	5.107	4.993	4.884	4.700	4.195	3.132	2.105	5.975	5.842	5.715	5.499	4.909	3.665	2.463
	10	3.534	3.417	3.219	2.972	2.362	2.103	1.500	4.135	3.983	3.766	3.108	2.763	2.170	1.755
$\alpha = 0.1$	0	19.708	18.814	17.955	17.115	16.293	15.489	14.705	23.058	22.013	21.007	20.024	19.063	18.123	17.204
	3	4.643	4.539	4.440	4.273	3.814	2.848	1.914	5.432	5.311	5.195	4.999	4.462	3.332	2.239
	10	3.213	3.106	2.926	2.702	2.147	1.912	1.364	3.759	3.621	3.424	2.825	2.512	1.973	1.596
$\alpha = 0.2$	0	15.160	14.472	13.812	13.165	12.533	11.915	11.311	17.737	16.933	16.160	15.403	14.664	13.940	13.234
	3	3.571	3.492	3.416	3.287	2.934	2.190	1.472	4.178	4.085	3.996	3.846	3.433	2.563	1.722
	10	2.471	2.389	2.251	2.079	1.651	1.471	1.049	2.891	2.786	2.634	2.173	1.932	1.518	1.228

References

[1] Gaspar JSD, Loja MAR, Barbosa JI. Static and free vibration analyses of functionally graded plane structures. J Compos Sci 2023;7(9):377.

[2] Chen D, Gao K, Yang J, Zhang L. Functionally graded porous structures: analyses, performances, and applications–a review. Thin-Walled Struct 2023;191:111046.

[3] An J, Wang A, Zhang K, Zhang W, Song L, Xiao B, et al. Bending and buckling analysis of functionally graded graphene origami metamaterial irregular plates using generalized finite difference method. Results Phys 2023;53:106945.

[4] Yu P, Leng W, Peng L, Suo Y, Guo J. The bending and vibration responses of functionally graded piezoelectric nanobeams with dynamic flexoelectric effect. Results Phys 2021;28:104624.

[5] Wang Y, Zhou A, Xie K, Fu T, Shi C. Nonlinear static behaviors of functionally graded polymer-based circular microarches reinforced by graphene oxide nanofillers. Results Phys 2020;16:102894.

[6] Karami B, Janghorban M, Li L. On guided wave propagation in fully clamped porous functionally graded nanoplates. Acta Astronaut 2018;143:380–90.

[7] Ebrahimi F, Daman M, Jafari A. Nonlocal strain gradient-based vibration analysis of embedded curved porous piezoelectric nano-beams in thermal environment. Smart Struct Syst 2017;20(6):709–28.

[8] Yüksel YZ, Akbaş ŞD. Buckling analysis of a fiber reinforced laminated composite plate with porosity. J Comput Appl Mech 2019;50(2):375–80.

[9] Berghouti H, Adda Bedia EA, Benkhedda A, Tounsi A. Vibration analysis of nonlocal porous nanobeams made of functionally graded material. Adv Nano Res 2019;7(5):351–64.

[10] Kiarasi F, Babaei M, Mollaei S, Mohammadi M, Asemi K. Free vibration analysis of FG porous joined truncated conical-cylindrical shell reinforced by graphene platelets. Adv Nano Res 2021;11(4):361–80.

[11] Akbaş ŞD, Bashiri AH, Assie AE, Eltaher MA. Dynamic analysis of thick beams with functionally graded porous layers and viscoelastic support. J Vib Control 2021;27 (13–14):1644–55.

[12] Alnujaie A, Akbas SD, Eltaher MA, Assie A. Forced vibration of a functionally graded porous beam resting on viscoelastic foundation. Geomech Eng 2021;24(1): 91–103.

[13] Akbaş ŞD. Dynamic analysis of axially functionally graded porous beams under a moving load. Steel Compos Struct 2021;39(6):811–21.

[14] Alimoradzadeh M, Akbas SD. Nonlinear vibration analysis of carbon nanotube-reinforced composite beams resting on nonlinear viscoelastic foundation. Geomech Eng 2023;32(2):125–35.

[15] Bensaid I, Saimi A. Dynamic investigation of functionally graded porous beams resting on viscoelastic foundation using generalised differential quadrature method. Aust J Mech Eng 2023;21(4):1440–59.

[16] Bentrar H, Chorfi SM, Belalia SA, Tounsi A, Ghazwani MH, Alnujaie A. Effect of porosity distribution on free vibration of functionally graded sandwich plate using the P-version of the finite element method. Struct Eng Mech 2023;88(6):551–67.

[17] Bourada F, Bousahla AA, Tounsi A, Tounsi A, Tahir SI, Al-Osta MA, et al. An integral quasi-3D computational model for the hygro-thermal wave propagation of imperfect FGM sandwich plates. Comput Concr 2023;32(1):61–74.

[18] Addou FY, Bourada F, Meradjah M, Bousahla AA, Tounsi A, Ghazwani MH, et al. Impact of porosity distribution on static behavior of functionally graded plates using a simple quasi-3D HSDT. Comput Concr 2023;32(1):87–97.

[19] Alsubaie AM, Alfaqih I, Al-Osta MA, Tounsi A, Chikh A, Mudhaffar IM, et al. Porosity-dependent vibration investigation of functionally graded carbon nanotube-reinforced composite beam. Comput Concr 2023;32(1):75–85.

[20] Khorasani M, Lampani L, Tounsi A. A refined vibrational analysis of the FGM porous type beams resting on the silica aerogel substrate. Steel Compos Struct 2023;47(5):633–44.

[21] Mesbah A, Belabed Z, Amara K, Tounsi A, Bousahla AA, Bourada F. Formulation and evaluation a finite element model for free vibration and buckling behaviours of functionally graded porous (FGP) beams. Struct Eng Mech 2023;86(3):291–309.

[22] Katiyar V, Gupta A, Tounsi A. Microstructural/geometric imperfection sensitivity on the vibration response of geometrically discontinuous bi-directional functionally graded plates (2D FGPs) with partial supports by using FEM. Steel Compos. Struct 2022;45(5):621–40.

[23] Cuong-Le T, Nguyen KD, Le-Minh H, Phan-Vu P, Nguyen-Trong P, Tounsi A. Nonlinear bending analysis of porous sigmoid FGM nanoplate via IGA and nonlocal strain gradient theory. Adv Nano Res 2022;12(5):441–55.

[24] Xia L, Wang R, Chen G, Asemi K, Tounsi A. The finite element method for dynamics of FG porous truncated conical panels reinforced with graphene platelets based on the 3-D elasticity. Adv Nano Res 2023;14(4):375–89.

[25] Belabed Z, Tounsi A, Al-Osta MA, Tounsi A, Minh HL. On the elastic stability and free vibration responses of functionally graded porous beams resting on Winkler-pasternak foundations via finite element computation. Geomech Eng 2024;36(2): 183–204.

[26] Chitour M, Bouhadra A, Bourada F, Mamen B, Bousahla AA, Tounsi A, et al. Stability analysis of imperfect FG sandwich plates containing metallic foam cores under various boundary conditions. Structures 2024;61:106021.

[27] Chen D, Rezaei S, Rosendahl PL, Xu BX, Schneider J. Multiscale modelling of functionally graded porous beams: buckling and vibration analyses. Eng Struct 2022;266:114568.

[28] Zhao S, Zhang Y, Zhang Y, Zhang W, Yang J, Kitipornchai S. Buckling of functionally graded hydrogen-functionalized graphene reinforced beams based on machine learning-assisted micromechanics models. Eur J Mech-A/solids 2022;96: 104675.

[29] Akgöz B, Civalek Ö. Buckling analysis of functionally graded tapered microbeams via Rayleigh-Ritz method. Mathematics 2022;10(23):4429.

[30] Hosseini SMH, Arvin H, Kiani Y. On buckling and post-buckling of rotating clamped-clamped functionally graded beams in thermal environment. Mech Based Des Struct Mach 2022;50(8):2779–94.

[31] Elkafrawy M, Alashkar A, Hawileh R, Al Hamaydeh M. FEA investigation of elastic buckling for functionally graded material (FGM) thin plates with different hole shapes under uniaxial loading. Buildings 2022;12(6):802.

[32] Zhao S, Zhang Y, Wu H, Zhang Y, Yang J. Functionally graded graphene origami-enabled auxetic metamaterial beams with tunable buckling and postbuckling resistance. Eng Struct 2022;268:114763.

[33] Van Do T, Hong Doan D, Chi Tho N, Dinh Duc N. Thermal buckling analysis of cracked functionally graded plates. Int J Struct Stab Dyn 2022;22(8):2250089.

[34] Chang X, Zhou J. Static and dynamic characteristics of post-buckling of porous functionally graded pipes under thermal shock. Compos Struct 2022;288:115373.

[35] Liu L, Liu A, Yang J, Fu J. Lateral-torsional buckling of functionally graded porous arches with graphene platelets reinforcements under an arbitrary radial concentrated load. Compos Struct 2022;281:114973.

[36] Turan M, Uzun Yaylacı E, Yaylacı M. Free vibration and buckling of functionally graded porous beams using analytical, finite element, and artificial neural network methods. Arch Appl Mech 2023;93(4):1351–72.

[37] Turan M, Adiyaman G. Free vibration and buckling analysis of porous two-directional functionally graded beams using a higher-order finite element model. J Vib Eng Technol 2023;12:1133–52.

[38] Derikvand M, Farhatnia F, Hodges DH. Functionally graded thick sandwich beams with porous core: buckling analysis via differential transform method. Mech Based Des Struct Mach 2023;51(7):3650–77.

[39] Wang S, Ding W, Li Z, Xu B, Zhai C, Kang W, et al. A size-dependent quasi-3D model for bending and buckling of porous functionally graded curved nanobeam. Int J Eng Sci 2023;193:103962.

[40] Truong TT, Lee S, Lee J. An artificial neural network-differential evolution approach for optimization of bidirectional functionally graded beams. Compos Struct 2020;233:111517.

[41] Nguyen-Xuan H, Tran LV, Thai CH, Kulasegaram S, Bordas SPA. Isogeometric analysis of functionally graded plates using a refined plate theory. Compos B Eng 2014;64:222–34.

[42] Wang Q, Li Q, Wu D, Yu Y, Tin-Loi F, Ma J, et al. Machine learning aided static structural reliability analysis for functionally graded frame structures. App Math Model 2020;78:792–815.

[43] Lieu QX, Lee J. A reliability-based optimization approach for material and thickness composition of multidirectional functionally graded plates. Compos B Eng 2019;164:599–611.

[44] Alsaleem SM, Wright LM, Han JC. Heat transfer and friction in a Rectangular Channel with Varying numbers of walls roughened with 90-deg transverse or 45-deg V-shaped ribs. ASME J Heat Mass Transfer 2023;145(2):023901.

[45] Zhang Y, Xu X, Liu S, Chen T, Hu Z. Crashworthiness design for bi-graded composite circular structures. Constr Build Mater 2018;168:633–49.

[46] Fujii T, Murakami R, Kobayashi N, Tohgo K, Shimamura Y. Uniform porous and functionally graded porous titanium fabricated via space holder technique with spark plasma sintering for biomedical applications. Adv Powder Technol 2022;33 (6):103598.

[47] Su L, Liu H, Yao G, Zhang J. Experimental study on the closed-cell aluminum foam shock absorption layer of a high-speed railway tunnel. Soil Dyn Earthq Eng 2019; 119:331–45.

[48] Bridjesh P, Geetha NK, Ch R, Nagaraju S. On numerical buckling analysis of two directional porous functionally graded beam using higher order shear deformation theory. Acad J Manuf Eng 2023;21(1):105–19.

[49] Reedy G, Geetha NK, Ravikiran C, Nagaraju S. On Numerical bending analysis of functionally graded porous beam-effect of porosity adapting higher order Shear deformation theory. J Comput Appl Mech 2023;54(1):49–67.

[50] Mehdianfar P, Shabani Y, Khorshidi K. Natural frequency of sandwich beam structures with two dimensional functionally graded porous layers based on novel formulations. Int J Eng 2022;35(11):2092–101.

[51] Bridjesh P, Geetha NK, Yelamasetti B. Numerical investigation on buckling of two-directional porous functionally graded beam using higher order shear deformation theory. Int J Interact Des Manuf 2023;1–14.

[52] O'Connor P, Kleyner A. Practical reliability engineering. John Wiley & Sons; 2012.

[53] Duer S, Woźniak M, Paś J, Zajkowski K, Bernatowicz D, Ostrowski A, et al. Reliability testing of wind farm devices based on the mean time between failures (MTBF). Energies 2023;16(4):1659.

[54] Ren H, Chen X, Chen Y. Reliability based aircraft maintenance optimization and applications. Academic Press; 2017.

[55] Pedroso DM. FORM reliability analysis using a parallel evolutionary algorithm. Struct Saf 2017;65:84–99.

[56] Kioko MM, Odhong EV, Ondieki CM. Optimization of parameters of plastic grinding machine using generalized reduced gradient non-linear programming. Int J Adv Manuf Technol 2023;129:421–7.

[57] Roudak MA, Karamloo M, Shayanfar MA. An iterative two-step Lagrangian-based method for evaluation of structural reliability index. Periodica Polytechnica Civil Engineering 2022;66(4):1207–19.

[58] Coit DW, Zio E. The evolution of system reliability optimization. Reliab Eng Syst Saf 2019;192:106259.

[59] Xu J, Zhu S. An efficient approach for high-dimensional structural reliability analysis. Mech Syst Sig Process 2019;122:152–70.

[60] Ray R, Kumar D, Samui P, Roy LB, Goh ATC, Zhang W. Application of soft computing techniques for shallow foundation reliability in geotechnical engineering. Geosci Front 2021;12(1):375–83.

[61] Song M, Cheng L. Solving the reliability-oriented generalized assignment problem by lagrangian relaxation and alternating direction method of multipliers. Expert Syst Appl 2022;205:117644.

[62] Chandramohan DL, Kanthasamy E, Gatheeshgar P, Poologanathan K, Ishqy MFM, Suntharalingam T, et al. Shear behaviour and design of doubly symmetric hollow flange beam with web openings. J Constr Steel Res 2021;185:106836.